(*The 39th International Workshop on Water Waves and Floating Bodies, 14-17 April 2024, St Andrews, Scotland*)

Upstream waves and wake waves induced by a travelling pressure distribution with dynamic correction

Jinyu Yao[1]*, Harry B. Bingham[2], Xinshu Zhang[1]

[1]State Key Laboratory of Ocean Engineering, Shanghai Jiao Tong University, Shanghai, China

[2]Department of Civil & Mechanical Engineering, Technical University of Denmark, Lyngby, Denmark

1 Introduction

Upstream solitons and wake waves are generated when a ship travels over a flat bottom with a near-critical or supercritical speed, which means the Froude number $Fr = U/\sqrt{gh}$ (where U is the ship speed, g is the acceleration of gravity and h is the water depth) is not less than 1. Wake waves, which show a V-shaped feature, comprise divergent waves and transverse waves. Based on the linear dispersion relation, the wake angle is found to be approximately 19.47° (Kelvin, 1887). To study the characteristics of ship-induced upstream solitons, a series of experiments were conducted by Ertekin *et al.* (1984). It was found that solitons are periodically generated at the bow, inducing periodic variation of the wave resistance. The crest line of the solitons is straight in a narrow channel, but curved in a wide channel (Li & Sclavounos, 2002). To investigate the transition from breaking solitons to a pure bore, Shi *et al.* (2018) proposed a fully nonlinear Boussinesq model combined with a shock-capturing dissipation scheme and a viscosity dissipation scheme, which can accurately predict the wave breaking at crests or steep fronts of solitons.

Mini-tsunami is a new type of upstream waves, which was observed by Grue (2017) in Norway. Mini-tsunamis are generated when a ship travels from deep to shallow water with a sub-critical speed ($Fr < 1$). The generation mechanism of mini-tsunamis can be attributed to the interaction between the bow and the variable topography (Grue, 2020). Mini-tsunamis observed in Norway have a wavelength ranging between 0.5-1 km and a maximum wave height of around 1.4 m, and can cause severe erosion on the coastlines. Nonlinear effects on mini-tsunamis are studied by Yao *et al.* (2023). Compared with linear results, second-order free-surface nonlinearities are able to more than double the wave amplitude of mini-tsunamis for a narrow channel at a large Froude number.

A moving static pressure distribution is one of the most common methods to simulate a travelling ship, and this method has been applied by many researchers (Huang & Wong, 1970; Doctors, 1972; Ertekin *et al.*, 1984; Yeung *et al.*, 2008; Grue, 2017; Shi *et al.*, 2018). However, in contrast to most previous work, a dynamic correction strategy for the static pressure distribution is used in the present paper to approximate a travelling ship. The dynamic correction strategy is shown to accurately maintain the desired ship geometry for a variety of test cases where a static pressure gives large deformations of the hull shape leading to significantly different wave patterns and resistance estimates.

2 High-order spectral model with dynamic correction

To simulate the evolution of nonlinear waves, the high-order spectral (HOS) model with a variable topography is used in the present study. This model has been adopted to solve many problems about nonlinear waves, such as the statistical characteristics of freak waves induced by the bathymetric variation (Gouin *et al.*, 2017), and the evolution of nonlinear ship-induced waves over a variable bottom (Yao *et al.*, 2023). The nonlinear free-surface boundary conditions are

$$\eta_t + \nabla\phi^S \cdot \nabla\eta - \phi_z(1 + \nabla\eta \cdot \nabla\eta) = 0, \quad \text{at } z = \eta, \tag{1}$$

$$\phi_t^S + g\eta + \frac{1}{2}\nabla\phi^S \cdot \nabla\phi^S - \frac{1}{2}\phi_z^2(1 + \nabla\eta \cdot \nabla\eta) = -\frac{p}{\rho}, \quad \text{at } z = \eta, \tag{2}$$

where $\phi^S(x, y, z, t) = \phi(x, y, \eta(x, y, t), t)$ is the potential on the free surface, $\nabla = (\frac{\partial}{\partial x}, \frac{\partial}{\partial y})$, ρ, g and p are the water density, gravitational acceleration and ship pressure distribution, respectively. The total water depth is expressed by $h = h_0 - \beta(x, y)$, where h_0 is the average water depth, β is a function for the depth variation. The potential ϕ and the free surface elevation η can be calculated from a Taylor expansion of ϕ around $z = 0$ truncated at order M, i.e. $\phi = \sum_{m=1}^{M} \phi^{(m)}$, and a Taylor expansion of the bottom boundary condition around

*Presenting author

$z = -h_0$ truncated at order M_b. The detailed solution process was introduced in Gouin *et al.* (2017). Here, we focus on the dynamic correction strategy for the moving pressure distribution p.

A travelling ship can be modeled by a moving pressure distribution $p(x, y, t)$, which is shown in the free-surface boundary condition Eq. (1). Based on the desired hull shape η_s, the static pressure distribution is defined as

$$p_s(x, y, t) = -\rho g \eta_s(x, y, t) = \rho g d f(x, t) q(y, t), \tag{3}$$

where the desired hull shape is approximated by two functions f and q, i.e.

$$f(x,t) = \begin{cases} \cos^2\left[\frac{\pi(|x-x^*(t)|-\frac{1}{2}\alpha L)}{(1-\alpha)L}\right] & \frac{1}{2}\alpha L \le |x - x^*(t)| \le \frac{1}{2}L \\ 1 & |x - x^*(t)| \le \frac{1}{2}\alpha L \end{cases}, \tag{4}$$

$$q(y,t) = \begin{cases} \cos^2\left[\frac{\pi(|y-y^*(t)|-\frac{1}{2}\beta B)}{(1-\beta)B}\right] & \frac{1}{2}\beta B \le |y - y^*(t)| \le \frac{1}{2}B \\ 1 & |y - y^*(t)| \le \frac{1}{2}\beta B \end{cases}. \tag{5}$$

The pressure is applied on the ship region defined by $-L/2 \le (x - x^*) \le L/2$ and $-B/2 \le (y - y^*) \le B/2$, where L and B are the ship length and width, respectively. d denotes the draft of ship. (x^*, y^*) is the center of the water plane of the ship. α and β are the coefficients controlling the shape of the wetted hull surface in the x and y directions, respectively (Shi *et al.*, 2018). In the present study, we apply a dynamic correction to this static pressure given by

$$p = -\rho g \eta_s + \rho g(\eta - \eta_s) - \frac{\rho}{2}\left[\nabla\phi^S \cdot \nabla\phi^S - \phi_z^2(1 + \nabla\eta \cdot \nabla\eta)\right] + \rho U(t)\frac{\partial \phi^S}{\partial x} \tag{6}$$

$$= -2\rho g \eta_s + \rho g \eta - \frac{\rho}{2}\left[\nabla\phi^S \cdot \nabla\phi^S - \phi_z^2(1 + \nabla\eta \cdot \nabla\eta)\right] + \rho U(t)\frac{\partial \phi^S}{\partial x}. \tag{7}$$

The first term in Eq. (6) is the static pressure and the rest of the terms are used for the dynamic correction.

Once the pressure is applied on the ship region, the potential ϕ and the free surface η can be time-stepped based on Eqs. (1) and (2). To control the sawtooth instabilities in the HOS model, the Savitzky-Golay filter is applied on free surface at each time step.

3 Results and discussion

3.1 Ship-induced waves over a flat topography

To investigate the generation and propagation of ship-induced solitons over a flat bottom, a series of experiments were conducted by Ertekin *et al.* (1984). The length, width and draft of the ship model are $L = 1.524$ m, $B = 0.234$ m and $d = 0.075$ m, respectively. The block coefficient $C_B = 0.8$. The ship model starts impulsively, and then travels along the centerline of the channel. To record the ship-induced waves, a wave gauge was placed 38.6 m in front of the initial position of the ship. The distance between the gauge and the channel wall is 0.23 m. In the numerical simulation, the order of free-surface nonlinearity in the HOS model is set to $M = 3$. The length of the computational domain is $L_x = 122.88$ m with the number of nodes $N_x = 8192$. The width of the computational domain L_y is equal to the channel width W, which changes in different test cases.

To validate the HOS model with dynamic correction, the amplitudes of the solitons computed by the numerical model and those in the experiments are compared in Figure 1, where the Froude number varies from 0.7 to 1.1, the water depth $h = 0.15$ m, and the channel width $W = 1.22$ m. The numerical results agree well with the experimental data, which gives confidence in the accuracy of the present method.

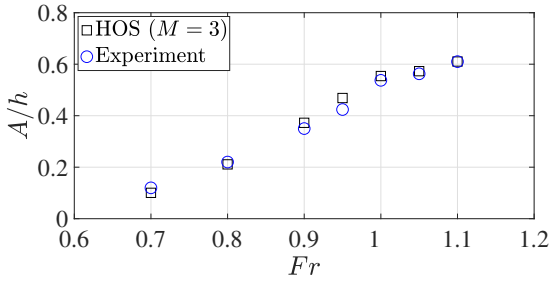

Figure 1: The variation of the non-dimensional amplitude A/h of the main upstream wave with the Froude number Fr. The water depth is $h = 0.15$ m. The channel width is $W = 1.22$ m. The black square denotes the numerical results obtained by using HOS ($M = 3$). The blue circle represents the experimental records in Ertekin *et al.* (1984).

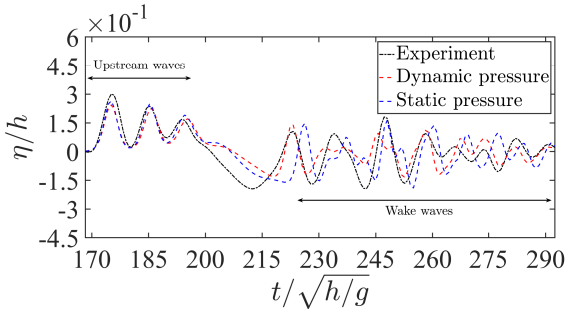

Figure 2: Comparison of the time series of the gauge records in the experiment of Ertekin *et al.* (1984) and those computed by the HOS model with a static pressure distribution and a dynamic pressure distribution. The water depth $h = 0.125$ m, the channel width $W = 4.88$ m, and the Froude number $Fr = 1$.

Table 1: Comparison of the resistance coefficients computed by the numerical models and those in the experiments. C_{wake} and C_{upstream} are the resistance coefficients induced by the wake waves and upstream waves, respectively. C_w is the coefficient of the total wave resistance. Calculation methods are indicated in parentheses. "WA", "FM", "PI" and "EXP" denotes "wave-cut analysis", "far-field method", "pressure integration" and "experiment", respectively. The experimental records are from Ertekin *et al.* (1984). The water depth $h = 0.15$ m, the channel width $W = 1.22$ m, and the Froude number $Fr = 1$.

Types of pressure distribution	C_{wake} (WA)	C_{upstream} (FM)	C_w ($C_{\text{wake}} + C_{\text{upstream}}$)	C_w (PI)	C_w (EXP)
Dynamic pressure	0.0952	0.6767	0.7719	0.7704	0.7588
Static pressure	0.1618	0.6744	0.8362	0.8416	

To investigate the effects of dynamic correction on ship-induced waves, the gauge records computed by the static and dynamic pressure distributions are compared with the experimental records in Figure 2. The water depth $h = 0.125$ m, the channel width $W = 4.88$ m, and the Froude number $Fr = 1$. Upstream solitons induced by the two types of moving pressure distribution are comparable to the experimental records. However, the wake waves are more sensitive to the dynamic correction. There are significant phase differences between the wake waves induced by the static pressure and those in the experiments. The wave amplitudes of wake waves between $260 \leq t/\sqrt{h/g} \leq 280$ from static pressure are larger than the experimental data. However, the wave amplitude and phase of the wake waves induced by the dynamic pressure are closer to the experimental results. A correlation coefficient ϵ is adopted to quantify the differences in the wake waves between the numerical and experimental results. $\epsilon = 0.6024$ for the dynamic pressure, while $\epsilon = 0.3750$ for the static pressure. This demonstrates that the dynamic correction strategy improves the accuracy in the simulation of wake waves.

As shown in Table 1, the wave resistance computed with the dynamic and static pressure is compared with the experimental records. Because of the differences in the amplitude of upstream waves and wake waves, the total resistance of the ship modeled by a static pressure distribution is approximately 10% larger than the experimental records. However, the results with the dynamic pressure distribution correspond well to the experimental records.

3.2 Mini-tsunamis over a variable topography

In the numerical simulation, the ship travels along the centerline of a channel with a variable topography. The length and width of the computational domain are $(L_x, L_y) = (300h_0, 3h_0)$, where h_0 is the average water depth. The number of nodes is $(N_x, N_y) = (8192, 512)$. The variation of the water depth along the x-axis is expressed as $\beta(x) = -\frac{1}{2}\Delta h_0 + \frac{1}{2}\Delta h_0 \left[\tanh\left(\gamma\left(x - x_a\right)\right) - \tanh\left(\gamma(x - x_b)\right)\right]$, where the ratio of the depth change and the average depth is $\Delta h_0/h_0 = 0.909$. The two centers of the depth variation are at $x_a = 90h_0$ and $x_b = 210h_0$, respectively. The ship length to ship width ratio is $L/B = 6$, the ship width to ship draft ratio is $B/d = 6$. The channel width to ship width ratio is $W/B = 4$.

Figure 3 shows the free surface in the ship region after the ship travels through the depth change. The ship hull modeled by the static pressure distribution has significant oscillation, while the ship modeled by the dynamic pressure has a flat bottom. This implies that the desired hull shape is preserved by the dynamic correction. The variation of the amplitude of mini-tsunamis with the Froude number based on the average water depth is shown in Figure 4. Because of the deformation of the bottom, the ship modeled by the static pressure distribution has a larger volume than that modeled by the dynamic pressure distribution. Therefore, the amplitude of mini-tsunamis induced by the dynamic pressure distribution is smaller than that induced by the static pressure distribution. The dynamic effects result from the movement of the ship. The larger the ship speed is, the faster the velocity field of fluids around the ship changes with time, and the more significant the effects of the dynamic pressure are. Therefore, the differences in wave amplitudes generated by the static and dynamic pressure distributions are more significant as the Froude number increases.

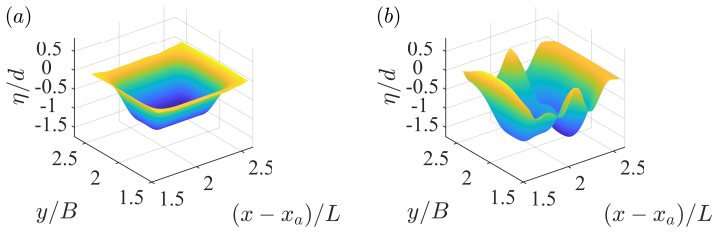

Figure 3: Free surface η in the ship region after the ship passed the bathymetric variation. The center of the depth change is denoted by x_a. The ship draft is denoted by d. The ships are modeled by the (a) dynamic pressure distribution and the (b) static pressure distribution, respectively.

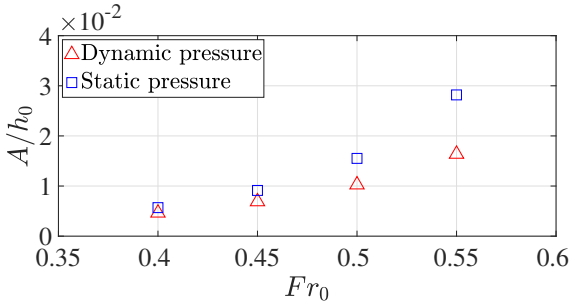

Figure 4: The variation of the non-dimensional amplitude A/h_0 of mini-tsunamis with the Froude number based on the average water depth Fr_0. The average water depth is denoted by h_0.

The variation of the wave resistance coefficient C_w as the ship travels from deep to shallow water is shown in Figure 5. The resistance increases when the mini-tsunamis are generated, and then decreases to a stable condition when the mini-tsunamis have separated from the bow. Therefore, a peak of resistance is shown near the end of the transition zone for the water depth. As the Froude number increases, the peak resistance increases, and the position of the peak is closer to the end of the transition zone.

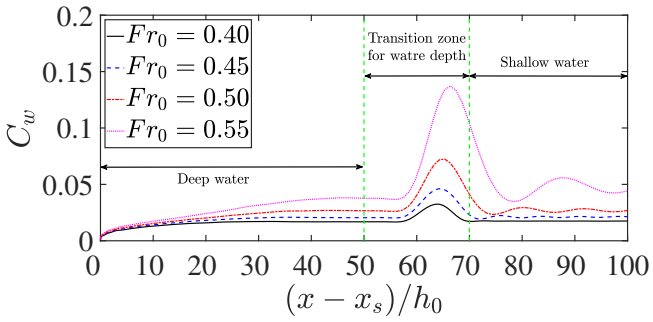

Figure 5: The variation of the wave resistance coefficient C_w as the ship travels from deep to shallow water. The resistance is calculated by the pressure integration method. x_s is the initial position of the ship.

References

Doctors, L. J. 1972 The wave resistance of an air-cushion vehicle in steady and accelerated motion. *J. Ship Res.* **16**, 248–260.

Ertekin, R. C., Webster, W. C. & Wehausen, J. V. 1984 Ship-generated solitons. In *Proc. 15th Symp. Nav. Hydrodyn. Hamburg*.

Gouin, M., Ducrozet, G. & Ferrant, P. 2017 Propagation of 3d nonlinear waves over an elliptical mound with a high-order spectral method. *Eur. J. Mech.-B* **63**, 9–24.

Grue, J. 2017 Ship generated mini-tsunamis. *J. Fluid Mech.* **816**, 142–166.

Grue, J. 2020 Mini-tsunami made by ship moving across a depth change. *J. Waterway, Port, Coastal, Ocean Eng.* **146** (5), 04020023.

Huang, T. T. & Wong, K. K. 1970 Disturbance induced by a pressure distribution moving over a free surface. *J. Ship Res.* **14** (3), 195–203.

Kelvin, L. 1887 On ship waves. In *Proc. Inst. Mech. Engrs.*, pp. 409–434. Edinburgh: Institution of Mechanical Engineers.

Li, Y. & Sclavounos, P. D. 2002 Three-dimensional nonlinear solitary waves in shallow water generated by an advancing disturbance. *J. Fluid Mech.* **470** (1), 383–410.

Shi, F., Malej, M., Smith, J. M. & Kirby, J. T. 2018 Breaking of ship bores in a Boussinesq-type ship-wake model. *Coastal Eng.* **132**, 1–12.

Yao, J., Bingham, H. B. & Zhang, X. 2023 Nonlinear effects of variable bathymetry and free surface on mini-tsunamis generated by a moving ship. *Phys. Rev. Fluids* **8**, 094801.

Yeung, R. W., Wan, H., Banumurthy, S. P., Ham, W. L. & Lew, J. M. 2008 Effects of configuration on wave resistance of multiple pressure distributions. *Mar. Syst. Ocean Technol.* **4** (2), 53–62.